University of Dundee

Investigation of the mechanisms on the abnormal features observed in thermal-mechanical testing of AA6061 under extrusion conditions

Zhang, Zhe; Tong, Chenpeng; Zhou, Wenbin; Jiang, Shuai; Lv, Jiaxin; Shi, Zhusheng

Investigation of the mechanisms on the abnormal features observed in thermal-mechanical testing of AA6061 under extrusion conditions

Zhe Zhang [a], Chenpeng Tong [a], Wenbin Zhou [b], Shuai Jiang [a], Jiaxin Lv [a], Zhusheng Shi [a,*], Jianguo Lin [a]

[a] *Department of Mechanical Engineering, Imperial College London, London, SW7 2AZ, UK*
[b] *School of Science and Engineering, University of Dundee, Dundee, DD1 4HN, UK*

ARTICLE INFO

ABSTRACT

Hot extrusion is the most common forming technology for aluminium alloy AA6061 due to its good extrudability, and thus it is important to study its high-temperature deformation characteristics. In this study, three abnormal features are observed in thermal-mechanical testing under extrusion conditions of AA6061 specimens from one billet: 1) Two types of specimens with grey-coloured surface or silver-coloured surface appear after solution heat treatment (SHT); 2) The silver-coloured specimens show orange peel surface after hot compression tests; 3) The silver-coloured specimens have lower flow stresses than the grey-coloured specimens. This paper investigates the mechanisms behind the above abnormal features. A laser scanning confocal microscope is employed to examine the surface roughening, and electron back scatter diffraction is used to characterise microstructural changes. It is found that the main causes of the above behaviour are due to different initial grain morphologies and the evolution of dislocation density after SHT. The silver-coloured specimens initially have smaller columnar grains which undergo recrystallisation and extensive growth during SHT, and the dislocation density decreases significantly, leading to orange peel defect and low flow stress during compression tests, respectively. The grey-coloured specimens have larger columnar grains. After SHT, some grains undergo recrystallisation, but others still maintain the shape of the large columnar grains, and the dislocation density does not change significantly, resulting in surface oxidation with smooth surface after thermal-mechanical testing and 10–25 MPa (30–50%) higher flow stress compared to the silver-coloured specimens in compression tests.

1. Introduction

Aluminium alloys are extensively applied in many fields, such as automotive, aerospace, transportation, and structural sectors, due to their advantages of light weight, excellent mechanical properties, good corrosion resistance and recyclability [1]. Extruded AA6061 is one of the most commonly used commercial aluminium alloys, particularly in yacht masts, angles and T sections within the civil and transport industries [2].

During extrusion, the microstructure of the alloy changes, affecting its mechanical properties. Both the dimensional accuracy and mechanical performance of the final products are dependent on the hot extrusion process. Therefore, gaining a comprehensive understanding of the hot deformation behaviour of the material becomes crucial for controlling the forming process and thus achieving high-quality products [3, 4]. However, the metal flow during hot deformation is complex since

both work hardening and dynamic softening (i.e. dynamic recovery (DRV) and dynamic recrystallisation (DRX)) are significantly affected by deformation parameters such as strain rate, temperature and deformation degree [5,6]. In addition, the ultimate performance of the material is influenced by the deformation conditions which affect the microstructural evolution of aluminium alloys [7,8]. Recent studies have explored the thermomechanical properties of different aluminium alloys under different loading conditions. Li et al. [9] investigated the thermomechanical properties of AA7050 under hot forging conditions and identified its high viscoplastic behaviour, where a suitably low strain rate and high temperature are beneficial to dynamic recrystallisation. Ebrahimi et al. [10] studied the thermal-mechanical properties of aluminium alloy 2024, observing an increase in flow stress with increasing strain rate. Furthermore, Fan et al. [11] studied the hot deformation behaviours of AA6061 and noted the presence of both dynamic recrystallisation and dynamic precipitation. They also found that

temperature has a significant impact on dynamic precipitation, where the increase in temperature suppresses dynamic precipitation as the second phases dissolve into the matrix. Despite much research on the hot deformation behaviours of aluminium alloys, there remains a lack of studies focusing on the surface features that occur during the hot deformation process.

Surface roughening during deformation is a common defect in aluminium alloys. Generally, surface roughening is considered to be associated with grain size and plastic heterogeneity under loading conditions. Raabe et al. [12] proposed three forms of surface defects: orange peel, ridging and roping. They suggested that orange peel is caused by the out-of-plane displacement of a single grain, while ridging and roping result from the collective deformation of grains with similar orientations. The orange peel phenomenon in metal forming processes has a significant negative impact on the product performance and production control. During the process, slip lines merge into blocky protrusions as the strain increases, causing out-of-plane displacements of grains and resulting in an uneven surface resembling orange peel [12]. Some studies have been conducted on orange peel occurrence in aluminium alloy deformation. Cai et al. [13] quantitatively investigated orange peel in 6063 alloy spun tubes, identifying a critical strain for different grain sizes of materials below which orange peel would not occur. Lo and Horng [14] observed a linear relationship between the roughness and the strain during plastic deformation of an AA1050-O plate, with minimal influence from strain rate. Conversely, Yang et al. [15] demonstrated a correlation between the surface roughness and the strain rates in 2060-T8 aluminium-lithium alloy. They found that the orange peel would appear earlier as the strain rate increases during tensile tests. However, all the above studies are under tensile deformation and there is a lack of research on characterising orange peel surfaces during hot compression deformation processes. Exploring this phenomenon in hot compression deformation would cover a more comprehensive understanding and help optimising processing parameters for specific forming processes, such as extrusion.

There are various factors that can affect the orange peel phenomenon, divided into intrinsic factors and extrinsic factors. Intrinsic factors include grain size, grain orientations, texture, crystal structure, surface layer modification, etc. [16]. Extrinsic factors include strain accumulation, strain rate, deformation conditions, etc. [17]. It is generally accepted that coarse grains lead to rough surfaces, and the surface roughness has a roughly linear relationship with the grain size [17,18]. Rittel and Roman [19] suggested that orange peel occurs when only one slip system is activated during the tensioning of cast coarse-grained Hadfield steels, especially for large-grained specimens. Zhao et al. [20] believed that the parallel distribution of different textures results in ridging and roping, while the random distribution of grain orientations is related to orange peel. Wouters et al. [21] studied the effect of crystal structure on the surface roughness of deformed polycrystalline aluminium, iron and zinc, and found that roughness in zinc is more than aluminium and iron because the limited number of slip systems available in zinc results in large average differences in hardness between adjacent grains, and this local hardness difference between grains causes roughness. Emelianova et al. [22] discovered that the size of orange peel dimples correlates with the grain size in the surface layer, and finer grains exhibit smaller dimples and a greater number of dimples.

In this work, the deformation behaviour of aluminium alloy AA6061 under hot extrusion conditions was studied by conducting solution heat treatment (SHT) and subsequent hot compression tests (HCT) at different temperatures and strain rates. Three abnormal phenomena were observed, i.e. surface oxidation, different thermal-mechanical properties and orange peel defect. To explore the mechanisms behind these abnormal features, the surface roughness of specimens after HCT at different temperatures and strain rates was analysed with a laser scanning confocal microscope. Furthermore, the grain morphology and the geometrically necessary dislocations (GND) density of AA6061 in the initial state and after SHT were examined using electron backscatter

diffraction (EBSD). The data were analysed and used to investigate the origin of the abnormal features.

2. Experimental procedure

The material studied was an AA6061 alloy whose main chemical compositions are 0.6Si, 0.9Mg, 0.5Fe, 0.3Cu, 0.1Mn, 0.1Cr, 0.1Zn, 0.1Ti (in wt. %). The as-received material was a homogenised billet with a diameter of 150 mm and a height of 210 mm. The billet was machined into cylindrical specimens (named initial specimens) with 8 mm in diameter and 12 mm in height for hot compression tests, as shown in Fig. 1. These specimens were solution heat treated (named SHTed specimens), and subsequently hot compression tested (named HCTed specimens) at various deformation temperatures and strain rates to study the thermal-mechanical behaviour of AA6061 under hot extrusion conditions.

Fig. 2 shows schematically the thermal history of the material. The specimens were SHTed at 530 °C for 1 h in an Instron furnace, followed by immediate water quenching to room temperature. Hot compression tests were carried out using Gleeble 3800 thermal-mechanical simulation system, at temperatures of 440, 460, 480 and 500 °C, and strain rates of 0.01, 0.1, and 1 s^{-1}. During hot compression tests, the specimens were firstly heated up with a heating rate of 5 °C/s to the target temperature and held for 3 min, and then compressed from 12 mm to 6.6 mm in height, followed by water quenching to room temperature.

The diameter change of the specimen was measured by C-gauge and the load was recorded by the test system. The true strain ε and true stress σ were calculated using the following equations:

$$\varepsilon = 2 \ln\left(\frac{D_0}{D}\right) \tag{1}$$

$$\sigma = \frac{4F}{\pi D^2} \tag{2}$$

where D_0 and D are respectively the initial diameter and the current diameter of the specimen in the test, F is the applied load recorded by the Gleeble machine.

Surface roughness and microstructure of the specimens were examined in this study. The surfaces of specimens after compression tests were examined using a TESCAN scanning electron microscope (SEM) and an Olympus OLS5000-SAF laser scanning confocal microscope to characterise surface roughening. The initial and SHTed specimens were cut along the cylinder axis (Fig. 1), and then the XY specimen in the centre of the cutting plane and the XZ specimen in the centre of the top plane of the cylinder were respectively taken to prepare the samples for EBSD. EBSD was employed to analyse the grain size and geometrically
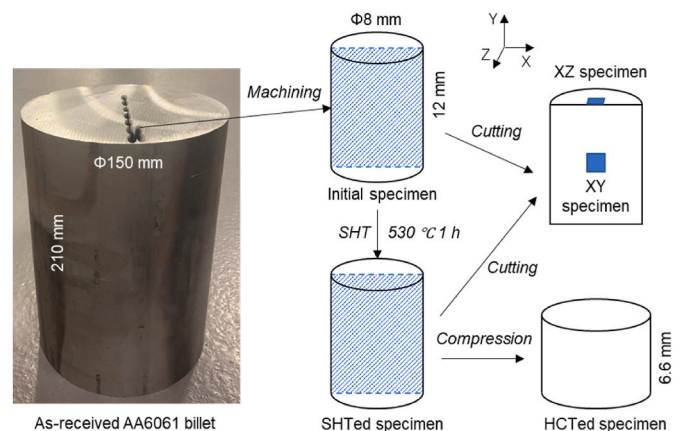

Fig. 1. Schematic of initial, SHTed and HCTed AA6061 specimens, and XY and XZ specimens after cutting.
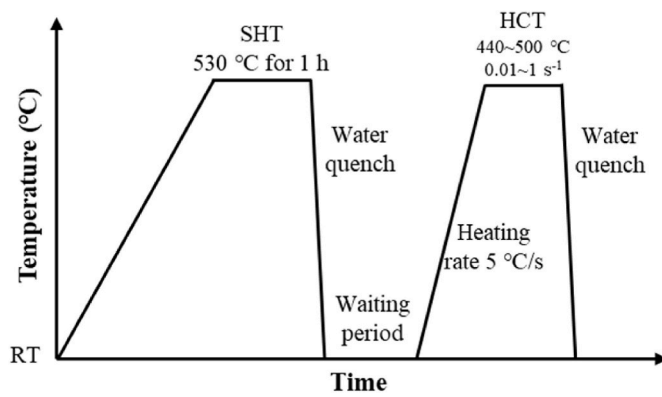
Fig. 2. Temperature profile for solution heat treatment and thermomechanical tests of as-received AA6061. RT: Room temperature; SHT: Solution heat treatment; HCT: Hot compression test.

necessary dislocations (GND) density in specimens. These smaller specimens were mechanically ground with sandpaper (up to 4000 grit) and polished with diamond suspension (down to 1 μm), followed by electropolishing with an electrolyte of 92% ethanol and 8% perchloric acid under a voltage of 20 V for 30 s. Microstructural examination was carried out by EBSD which uses Oxford Symmetry detector in conjunction with the SEM (TESCAN). EBSD data were acquired under the following conditions: beam voltage of 25 kV, beam currency of 10 nA, working distance of 10 mm, step size of 1 μm, and map size of 1×1 mm. The average grain size is an equivalent circle diameter calculated by area weighted method. The average grain size and GND density of specimens were analysed with AZtecCrystal software. In this study, GND density can be used to represent the total dislocation density, because dislocation creep and cross-slip will wipe out many statistically stored dislocations under hot deformation, where most of the stored dislocations are low-energy GND [23].

3. Results

3.1. Surface oxidation

After the solution heat treatment and hot compression experiments, some abnormal phenomena appeared on the surface of the specimens, as shown in Fig. 3. The surface of all the initial specimens machined from the same AA6061 billet was silver and shining. After SHT, some specimens retained the silver appearance on their surfaces, while other specimens were oxidised and turned grey. For convenience, the former specimens will be named as silver-coloured (SC) specimens and the

latter ones as grey-coloured (GC) specimens. In addition, the surface of the GC specimen was smooth after hot compression test, while the SC specimens had an orange peel surface, which will be further characterised in Section 3.3.

3.2. Thermomechanical behaviour

Fig. 4 shows the true stress-strain curves of AA6061 for GC specimens and SC specimens, obtained from hot compression tests at different temperatures and strain rates. Generally, the flow stress decreases with increasing deformation temperature and decreasing strain rate. When the strain rate is increased from 0.01 to 1 s^{-1}, the flow stress is increased by around 30 and 40 MPa respectively for SC and GC specimens. When the temperature is raised from 440 to 500 °C, the flow stress is reduced by about 10 and 20 MPa respectively for SC and GC specimens. Besides, at the same temperature and strain rate, it is found that the trend of the flow stress curves of GC specimens and SC specimens is similar, but the value of true stress of GC specimens is about 10–25 MPa (30–50%) higher than that of SC specimens.

3.3. Surface roughening

The surface of initial specimens after machining has a roughness (R_a) of 2 μm, which remained after SHT. The method to calculate the surface roughness of the initial, SHTed and HCTed-GC specimens is based on the study of Feng et al. [17]. Fig. 5 shows the 3D surface figures of AA6061 specimens after SHT and HCT, obtained with the laser scanning confocal microscope. X, Y and Z-axes are consistent with the orientations depicted in Fig. 1. It is found that after the compression test at the same temperature and strain rate, the surface of the GC specimens is smooth, while the surface of the SC specimens is very uneven like orange peel.

In order to study the orange peel phenomenon of SC specimens compression tested at different temperatures and strain rates, the surface line along the length of each specimen is obtained, and the reference line is determined by selecting the lowest point of the depression on the surface line (marked with letters a, b, c, d, e and f) and fitting these lowest points with a polynomial, as shown in Fig. 6. Then, the reference line is set to 0 and the surface line unfolds as the reference line unfolds.

Fig. 7 shows the unfolded surface lines of the SC specimens after hot compression tests. From a macro perspective, at the same temperature, the degree of surface unevenness increases as the strain rate increases, while at the same strain rate, the specimen surfaces are not significantly different under different temperatures.

For the quantitative evaluation of surface roughening, the surface roughness R_a could be calculated using the equation [17]:
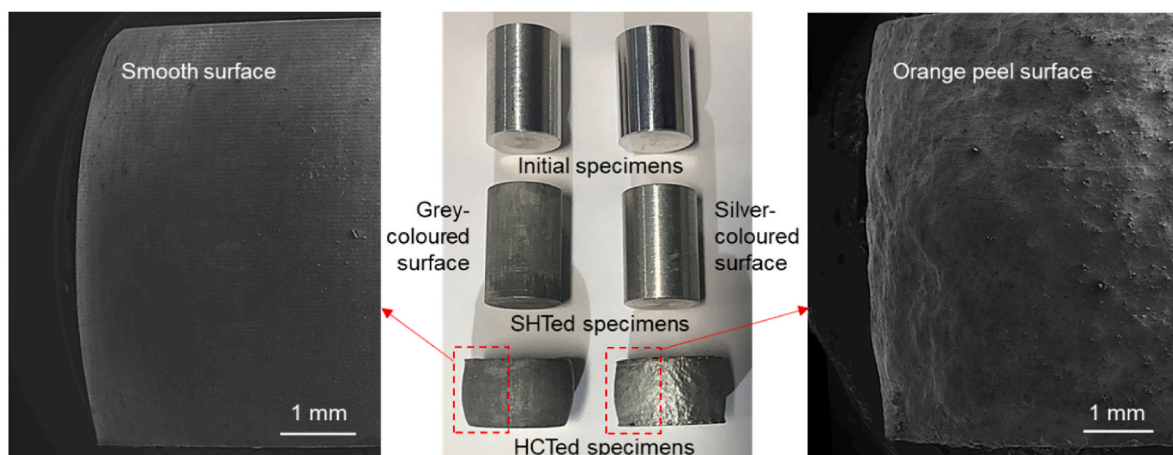

Fig. 3. Photographs of the initial, SHTed and HCTed AA6061 specimens, showing significantly different surface features.
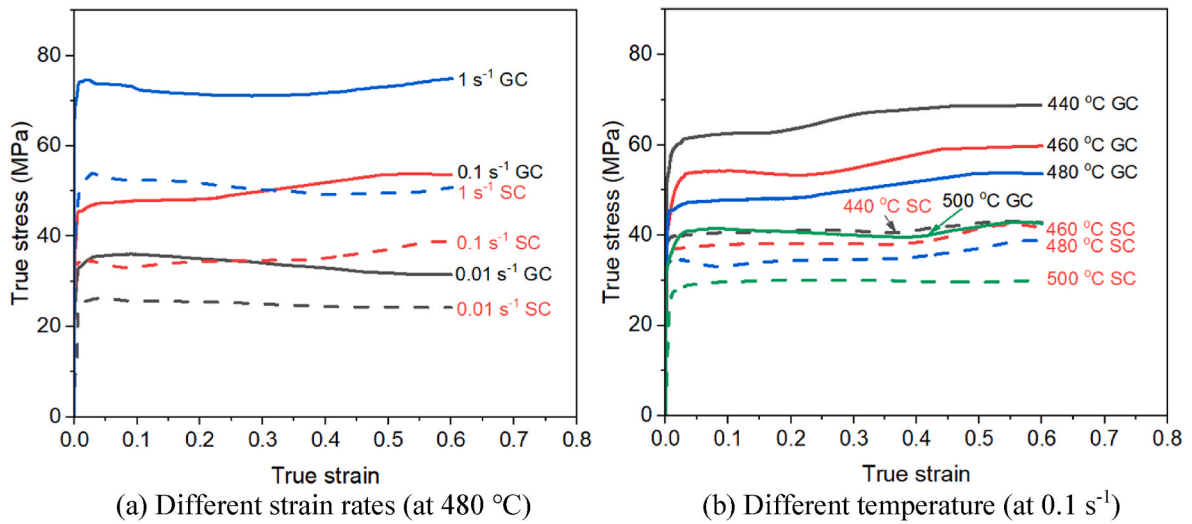
Fig. 4. Flow stresses of GC (solid curves) and SC (dash curves) AA6061specimens during HCT at different strain rates and temperatures. GC: Grey-coloured; SC: Silver-coloured.
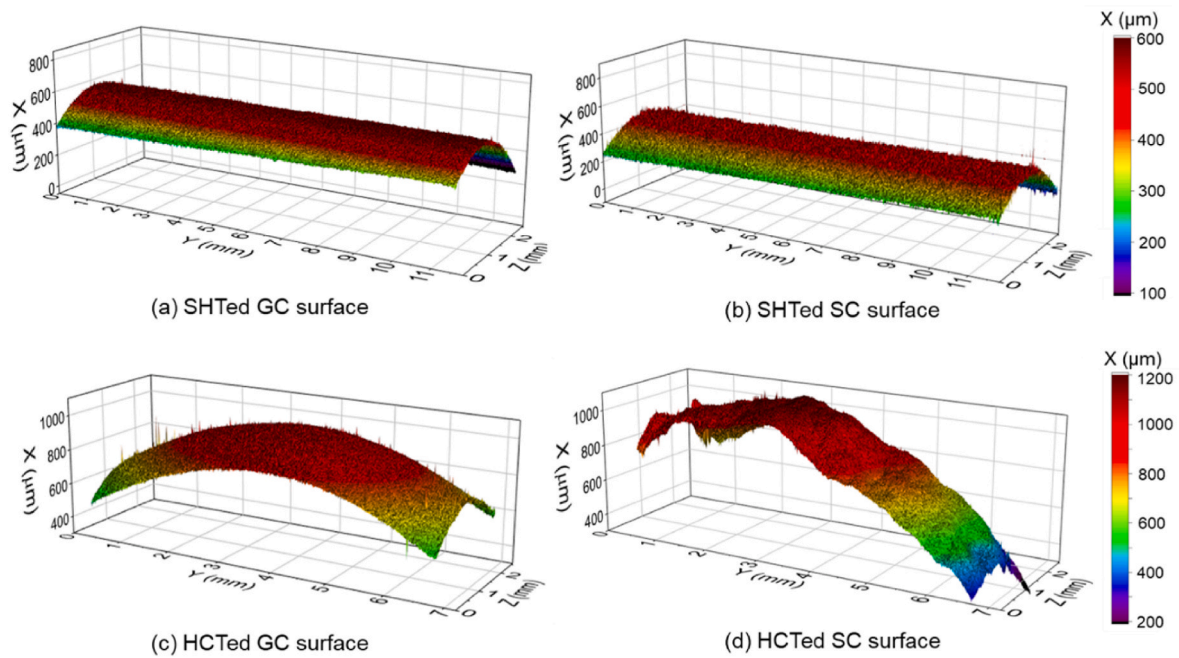

Fig. 5. The 3D surfaces of GC and SC specimens after HCT at 480 °C and 0.1 s^{-1}.
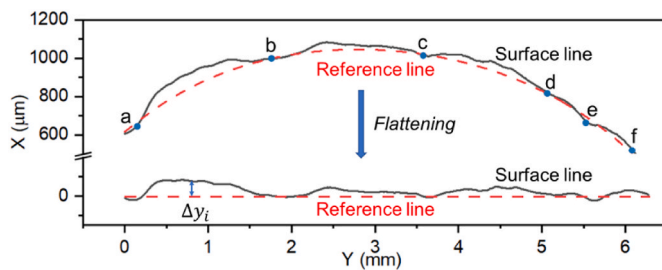
Fig. 6. Schematic of unfolding the surface line with orange peel. (For interpretation of the references to colour in this figure legend, the reader is referred to the Web version of this article.)

$$R_a = \frac{1}{n} \sum_{i=1}^{n} |\Delta y_i| \qquad (3)$$

where n is the number of sampling points in the length of the unfolded surface line swept, and $|\Delta y_i|$ is the deviation value of a sampling point of unfolded surface line from the unfolded reference line. The calculated surface roughness is shown in Fig. 8 for different compression test conditions.

At the same temperature, the surface roughness increases with increasing strain rate, as shown in Fig. 8a, and the values of R_a are 17.5, 18.4, and 22.6 μm, respectively for 0.01, 0.1, and 1 s^{-1} at 480 °C; while there is little change of R_a with increasing temperature at the same strain rate of 0.1 s^{-1} (Fig. 8b). In a word, the temperature has little effect on the orange peel of AA6061 aluminium alloy under compression tests, while the degree of orange peel increases with increasing strain rate.

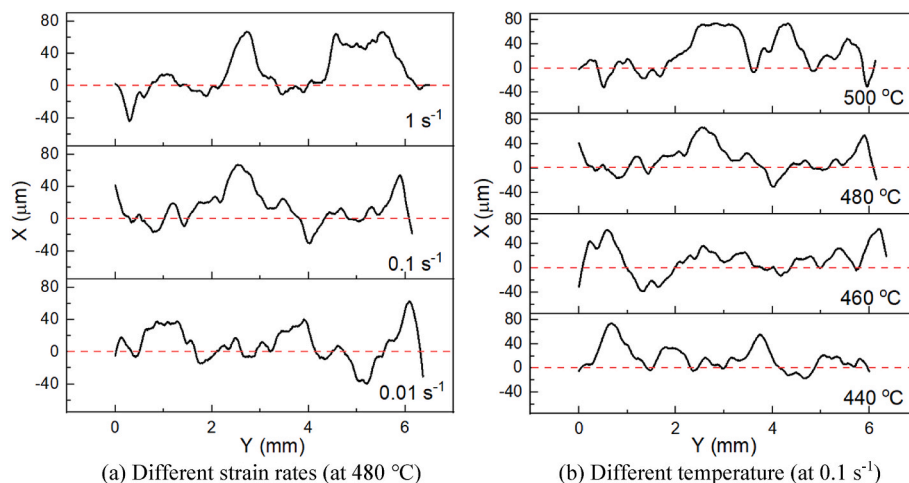(a) Different strain rates (at 480 °C)   (b) Different temperature (at 0.1 s⁻¹)

Fig. 7. Unfolded surface lines of compressed AA6061 SC specimens along Y (longitudinal) direction.

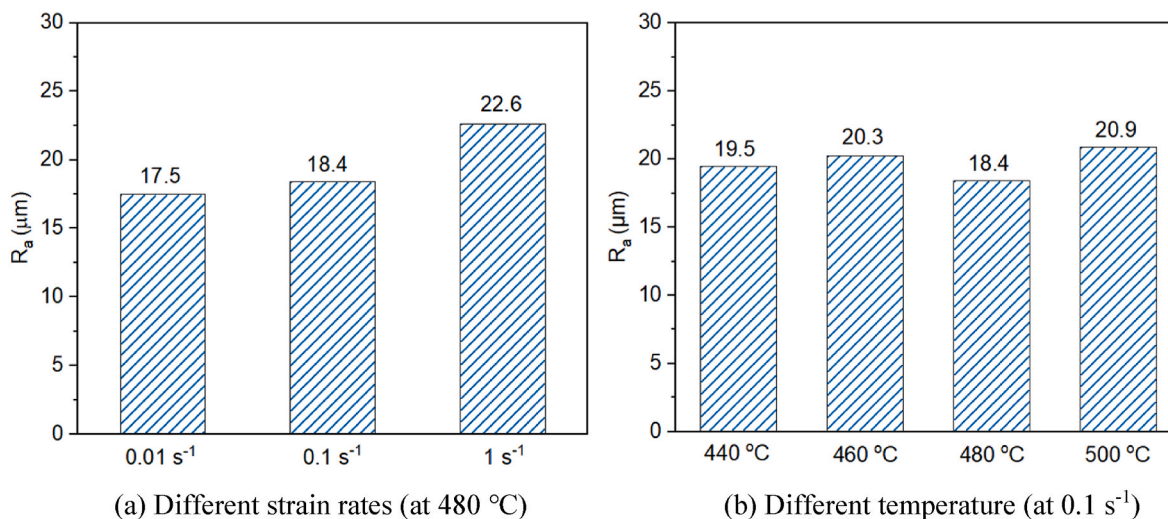(a) Different strain rates (at 480 °C)   (b) Different temperature (at 0.1 s⁻¹)

Fig. 8. Measured surface roughness of SC specimens compression tested with different temperatures and strain rates.

3.4. Grain morphology and GND

Fig. 9 shows the EBSD inverse pole figure (IPF) maps and their misorientation angle distribution of AA6061 XZ specimens (i.e. perpendicular to the billet axis) in the initial state and after SHT. The black lines indicate high-angle boundaries (HABs) with a misorientation angle of $\theta \geq 15°$, and the white lines represent low-angle boundaries (LABs) with a misorientation angle of $2° \leq \theta < 15°$. The percentages of HABs and LABs are also shown in the figures of misorientation angle distribution. For GC XZ specimens (Fig. 9a and b), the average grain sizes (*d*) are 119.2 and 120.5 μm for the initial and SHTed specimens, respectively. The grains of GC specimens barely grow and the HABs and LABs are almost unchanged after SHT. The distribution of misorientation angle for both GC XZ specimens (initial and SHTed states) has a similar trend, with a peak at near 2° misorientation and declining gradually until the 15° misorientation for LABs, and the misorientation angles of the HABs are concentrated in the range of 50°–60°. For initial and SHTed SC XZ specimens (Fig. 9c and d), the average grain sizes are 65.7 and 307.5 μm, respectively, showing huge increase in grain sizes. Compared with the GC specimens, the grains of the SC specimen are more uniform in both the initial and SHTed states. In terms of average grain size, the initial SC specimen has smaller grains (about half the size of GC specimens), but the grain size becomes about 2.5 times the size of GC specimens after SHT. For SC specimens, the number of LABs

decreased sharply after SHT (from 52.5% to 4.6%), which means that a larger number of sub-structural boundaries evolved into HABs. In addition, the initial SC specimens have a similar misorientation angle distribution to the GC specimens but have a higher peak population at around 2° misorientation and broader misorientation angle distribution of HABs. However, after SHT, the distribution of misorientation angle becomes random and is mostly in the high-angle area, as shown in Fig. 9d.

Fig. 10 shows the EBSD results (IPF maps and misorientation angle distribution) of GC and SC specimens at the initial state and after SHT for the XY sections (i.e. parallel to the billet axis). It is observed that the initial GC specimens have large columnar grains, while the initial SC specimens have small columnar grains. Since some columnar grains are longer than the EBSD analysis area, the grain size distribution does not have much meaning. Some large columnar grains in GC specimens have recrystallised during SHT and others do not change significantly. The LABs of GC specimens have been reduced by 15.9% (from 72.5% to 56.6%) after SHT due to the recrystallisation of some grains. For SC specimens, the final structure after SHT is large grains which have recrystallised and grown and low LABs fraction of only about 5%, similar to that in the XZ section. Furthermore, the trend of misorientation angle distribution of the initial GC specimens in XY plane is similar to that in XZ plane, while there is a little difference in SHTed GC specimens. The relative frequency of misorientation angle between 30° and
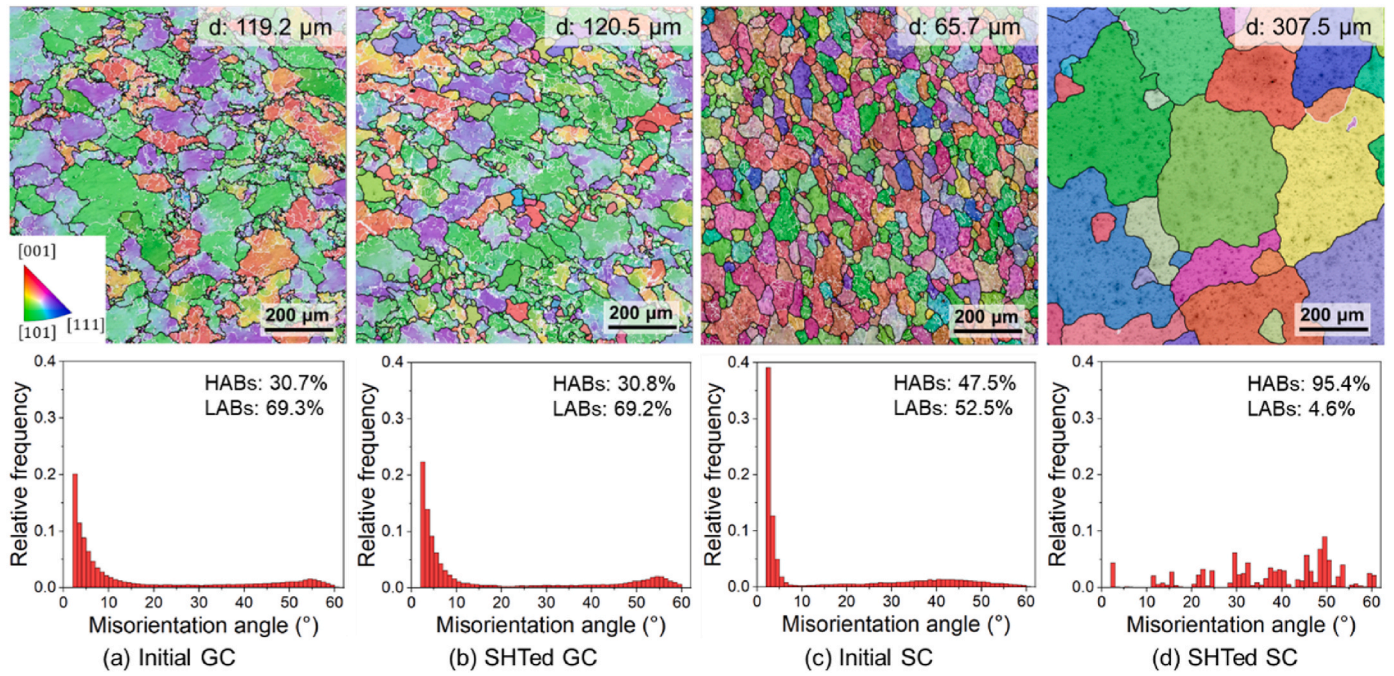
Fig. 9. EBSD IPF maps and the misorientation angle distribution of initial and SHTed XZ specimens, showing the grain structure with HABs (black lines) and LABs (white lines). The average grain size *d* and the fractions of HABs and LABs are given for each specimen.
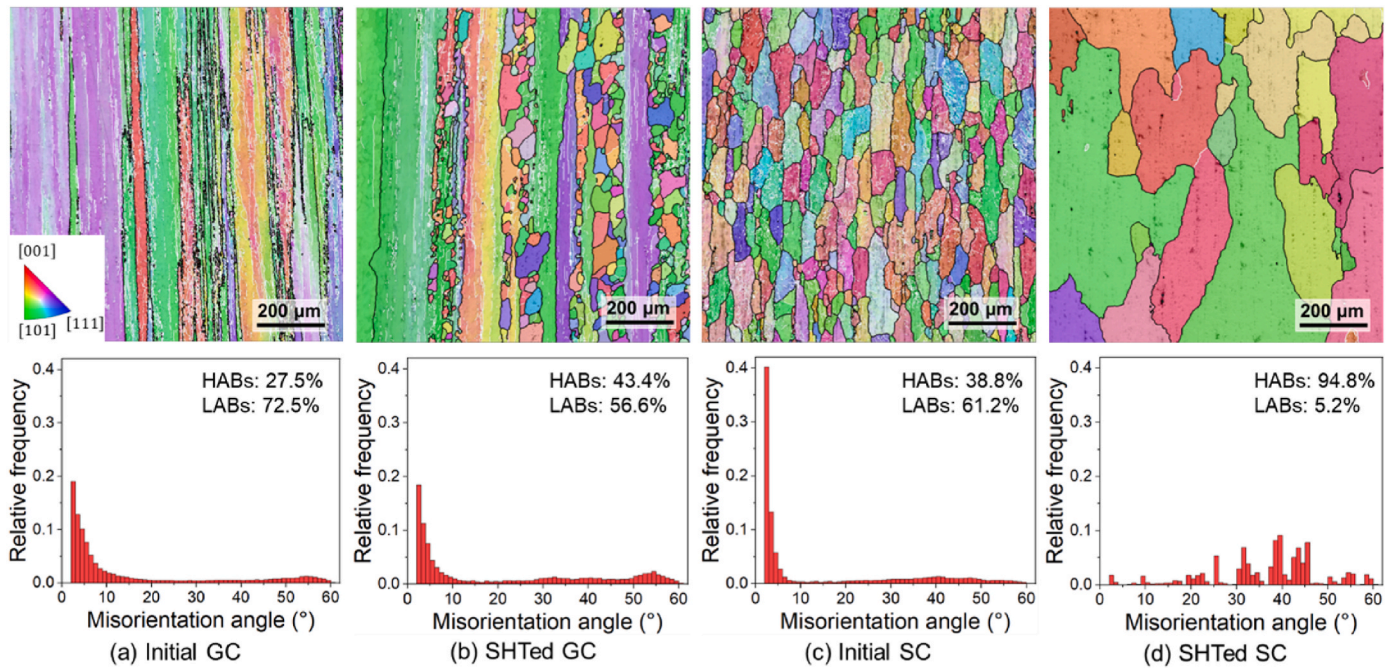

Fig. 10. EBSD IPF maps and the misorientation angle distribution of initial and SHTed XY specimens, showing the grain structure with HABs (black lines) and LABs (white lines) and their fractions.

$40°$ increases after SHT, implying that some recrystallised grains have been formed. For SC XY specimens, the evolution of HABs and LABs is consistent with that in the XZ specimens, where the number of LABs drops significantly from 61.2% to 5.2%. The distribution of misorientation angle of SC specimens in the XY plane after SHT is also random.

Combining the grain structure in the XZ and XY planes, it is shown that the initial GC specimens have larger columnar grains with large LABs, some grains undergo recrystallisation while others retain their original grain structure during SHT; the initial SC specimens have smaller columnar grains with relatively high LABs, but after SHT, the LABs are reduced significantly and the grain size becomes dramatically large. Besides, the SHTed SC specimens have random distribution of grain misorientation. These differences in grain structure evolution can explain the anomalies produced after SHT and compression tests.

Fig. 11 shows the GND density distribution in XY and XZ specimens of AA6061 in the initial state and SHTed state. One of the main drivers of recovery, recrystallisation and grain growth is the dislocation density [24]. It has been reported that GND density can be used to represent the
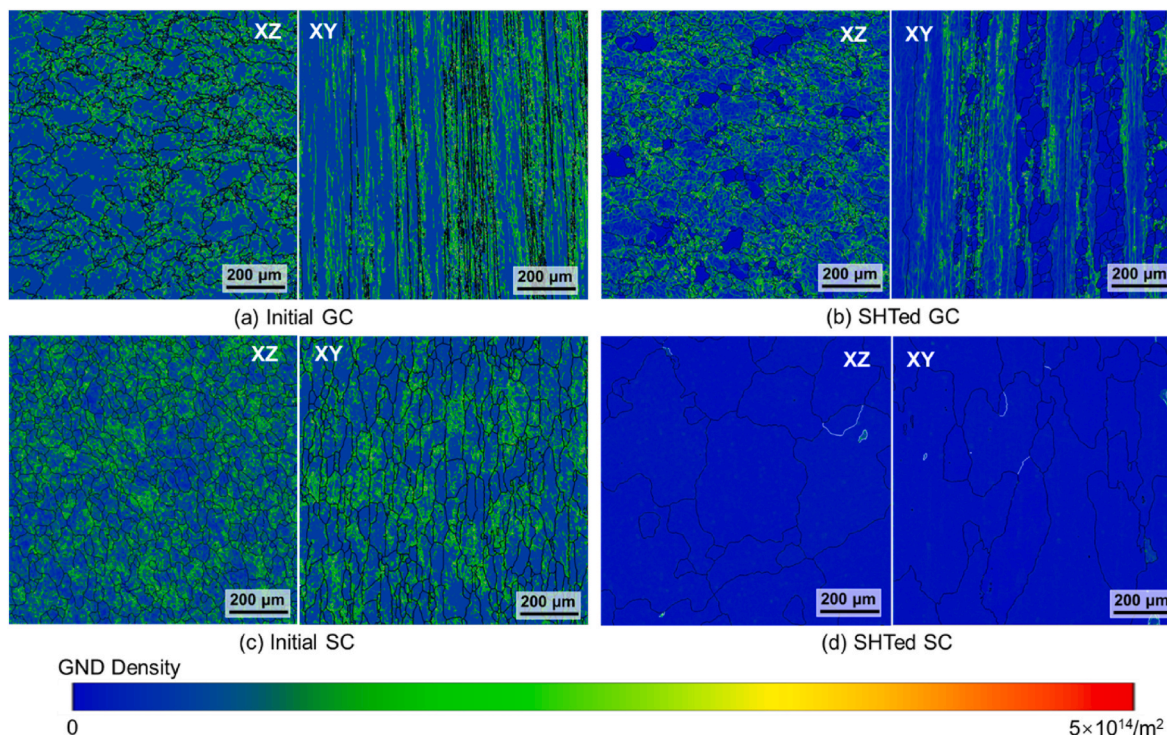
Fig. 11. GND distributions in the initial and SHTed AA6061 GC and SC specimens in the XZ and XY planes.

total dislocation density [20], which is adopted in this study. It can be seen that the GND density in the initial SC specimen is larger than that of the initial GC specimen. After SHT, however, the GND density in SC specimens drops sharply, to almost zero (Fig. 11d), indicating full recrystallisation. On the other hand, the GND density in GC specimens has a much less change and it can be observed that some recrystallised grains in SHTed GC specimens have low GND density (Fig. 11b).

In order to better compare the differences in GND density, the average GND density with error bars obtained from two tests of the individual specimen is calculated and shown in Fig. 12. The GND density of SC specimens in the XZ and XY planes decreases by 91% and 93%, respectively, but the GND density of GC specimen is just reduced by 20% and 26% respectively, which is associated with the fact that the grains of SC specimens are fully developed but the grains in GC specimens

Fig. 12. The average GND density values in initial and SHTed AA6061 GC and SC specimens in the XZ and XY planes.

scarcely grow.

4. Discussion

Three abnormal features were observed after the SHT and compression tests of the as-received AA6061 alloy, namely surface oxidation, different flow stresses, and orange peel appearance. These phenomena can be attributed to the different grain morphology, grain size and dislocation density in the specimens.

The initial SC specimens have smaller columnar grains while the initial GC specimens have larger columnar and irregular grains. The reason for the appearance of two grain structures is most likely because the as-received billet was not fully homogenised. During solution heat treatment, recrystallisation occurs in SC specimens and the dislocations inside the grains are greatly reduced, which means the energy inside the grains is released. After recrystallisation, grain growth occurs in SC specimens primarily through the migration of high-angle boundaries, and the curved boundaries tend to migrate towards the centres of curvature, which helps reduce the boundary energy. However, the initial GC specimens have large columnar grains surrounded with many fine grains, some grains undergo recrystallisation during SHT and there is only a modest amount of grain growth for some larger grains. In addition, columnar grains have a specific grain growth direction: the growth rate is faster along the longitudinal axis and slower in the lateral direction [25]. This characteristic can explain the limited growth of large columnar grains during SHT. After SHT, some recrystallised grains are observed along the grain boundary in GC specimens, due to the preferential nucleation at grain boundaries. It is known that the recrystallisation nucleation tends to occur at grain boundaries because of their high energy [26]. However, most areas in the GC specimens do not undergo complete recrystallisation within a SHT of 1 h and there are still many dislocations in the regions that have not recrystallised, as shown in Fig. 11b. These retained high dislocation density will affect the thermomechanical behaviour of the material, which will be further discussed later.

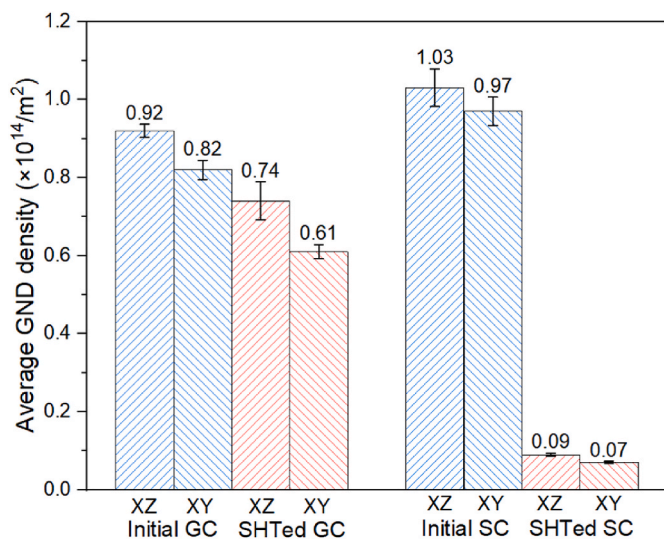The grey-coloured surface is due to oxidation and the colour changes

under different conditions. In general, the oxidised surface of aluminium alloys changes from silver to black as the thickness of oxidised layer increases [27,28]. The presence of water could hydrate the aluminium oxide film, thereby generating a hydrated oxide layer of greater thickness that would darken the colour of surface [29]. There are many factors that affect the surface oxidation of aluminium alloys, such as temperature, environment, grain size, etc. [30-32]. Most of the literature related to Al alloys seems to indicate that the oxidation susceptibility decreases as grain size decreases [33-35], but the opposite relationship is also observed [36,37]. In addition, it is reported that if larger residual stress remains, oxidation will increase [32,38]. In this study, all initial specimens have undergone the SHT with the same temperature (530 °C), the same duration (1 h) and the same environment, so the main factors which cause grey surface and silver surface are due to intrinsic reasons, such as dislocation density. It is found that the surface of GC specimens is more prone to oxidation than those SC specimens during water quenching process in SHT (Fig. 3). It is shown in Fig. 11 that after heat treatment, there are still a lot of dislocations in GC specimens due to limited recrystallisation, resulting in a higher susceptibility to oxidation. This is because dislocations have higher energies and are more active, which can increase the reactivity of the surface through increased electron activity and diffusion [32]. Compared with GC specimens, more dislocations in the initial SC specimens disappear during SHT, due to recovery and recrystallisation. Therefore, SC specimens have lower oxidation susceptibility and the surfaces remain bright.

The grain structure, grain size and dislocation density greatly influence the thermomechanical behaviours of aluminium alloys. In this study, there are two main reasons for the higher flow stress of GC specimens than that of SC specimens shown in Fig. 4. One is that grain boundary sliding and grain rotation are challenging to happen in GC specimens since they have large columnar grain morphology. In addition, before the hot compression tests, the dislocation density of GC specimens is much higher than that of SC specimens (Fig. 11b and d), being $0.68 \times 10^{14}/m^2$ and $0.08 \times 10^{14}/m^2$ in average respectively, which makes it more difficult for dislocation movement during the compression process, contributing to the increase of the flow stress. Therefore, the flow stress of GC specimens is higher than that of SC specimens. Another feature of thermomechanical behaviour is that the trends of flow stress for both types of specimens are similar. Various mechanisms, including work hardening, DRV, DRX, and dynamic grain growth, affect material's thermomechanical processes [39-41]. In this study, the flow stress curves initially exhibit a rapid rise followed by a decline or stabilisation before gradually rising again, as shown in Fig. 4 (strain rate of 0.1 and 1 s^{-1}). This behaviour can be attributed to the competition between work hardening and thermally activated process, which is consistent with previous research [42,43]. Work hardening leads to the initial increase in true stress by generating and accumulating dislocations, while DRV and DRX reduce the dislocation density and result in a decrease in flow stress [44].

Orange peel occurs when the crystals undergo individual out-of-plane displacements at the surface [12] and is one of surface roughening defects associated with plastic heterogeneities at grain-scale and loading conditions. It is commonly accepted that the coarse grains and the random distribution of grain orientations lead to orange peel [20,45]. The SC specimens after SHT have coarse grain size that is about 308 μm in the XZ plane and around 500 μm in the XY plane, and have random grain orientation distribution (Figs. 9d and 10d), which is easy for grains to carry out out-of-plane displacements during compression. On the other hand, the larger slender columnar crystals of GC specimens hardly undergo out-of-plane displacements when they are compressed. Therefore, after hot compression experiments, the surface of the SC specimens has the orange peel phenomenon but the surface of the GC specimens is smooth. Furthermore, it appears that prior dislocation density has little impact on the formation of orange peel during hot compression. As shown in Fig. 12, the GC specimens have higher dislocation density compared to SC specimens before the

thermomechanical tests, the orange peel phenomenon, however, is not observed in the GC specimens. In addition, the surface roughness increases with the increase of strain rate at the same temperature. This is because that, at low strain rates, grains have more time to recover during deformation, thereby the degree of orange peel and surface roughness is smaller; on the contrary, at high strain rates, there is insufficient time for grains to recover during deformation, and a large amount of strain energy is stored inside the grains, which increases the amount of deformation of the grains and the degree of inhomogeneity, leading to an increase in the degree of orange peel on the surface of the specimens. Besides, texture is also one of the factors that could affect orange peel phenomenon [16]. It has been reported that $\{001\}\langle110\rangle$ texture components could lead to the strong surface roughening, while the $\{011\}\langle110\rangle$ Goss and $\{011\}\langle110\rangle$ cube texture components have no effect on roughness evolution, showing a smooth free surface instead [16,46]. In this study, however, the main cause of orange peel is the grain morphology before deformation which determines whether the orange peel would occur during hot deformation.

In summary, billets that have not been fully homogenised can have abnormal phenomena during SHT and thermal deformation, such as surface oxidation, different flow stresses in different locations of the billet and orange peel, which will have an adverse impact on production and application. Therefore, aluminium alloy billets need be fully homogenised before extrusion to have uniform microstructure and properties.

5. Conclusions

In this study, three abnormal features of AA6061 aluminium alloy, namely surface oxidation, different thermomechanical behaviours, and orange peel surface, are observed after solution heat treatment and hot compression tests under extrusion conditions at different temperatures and strain rates. The mechanisms of these abnormal phenomena are analysed and discussed. The following conclusions can be drawn:

1. The initial grain morphology has a significant effect on the grain size and dislocation density evolution after SHT. Due to the large dislocation density and smaller columnar grains, the grains in the initial silver-coloured (SC) specimens recrystallise and grow from 65.7 to 307.5 μm during SHT, and the geometrically necessary dislocation (GND) density in the XZ and XY planes decrease sharply by 91% and 93%, respectively. However, the initial grey-coloured (GC) specimens have larger columnar grains, and only some grains undergo recrystallisation and the overall GND densities in other grains have much less reductions during SHT.

2. Specimens with higher dislocation density are more prone to oxidation during SHT. GC specimens are more susceptible to surface oxidation during SHT than SC specimens, due to higher GND densities in GC specimens (about $0.74 \times 10^{14}/m^2$ for XZ plane and $0.61 \times 10^{14}/m^2$ for XY plane) after SHT, compared with those for SC specimens (about $0.09 \times 10^{14}/m^2$ for XZ plane and $0.07 \times 10^{14}/m^2$ for XY plane).

3. The average true flow stress of GC specimens is about 10–25 MPa (30–50%) higher than that of SC specimens at the same temperature and strain rate because of the much higher dislocation density before hot compression tests and the large columnar grain structure which is difficult for grain boundary sliding and grain rotation to occur. The increase in flow stress is not favourable for hot extrusion.

4. Orange peel phenomenon occurs in the SC specimens after hot compression tests because they have coarse grains and random distribution of grain orientation. The surface roughness increases from 17.5 to 22.6 μm with the increase of strain rate from 0.01 to 1 s^{-1} at the same temperature, but it changes insignificantly with increasing temperature from 440 to 500 °C. Large columnar grain morphology (in GC specimens) does not result in orange peel during hot deformation.

CRediT authorship contribution statement

Zhe Zhang: Methodology, Investigation, Writing – original draft, Visualization. **Chenpeng Tong:** Investigation, Writing – review & editing. **Wenbin Zhou:** Writing – review & editing. **Shuai Jiang:** Methodology, Investigation. **Jiaxin Lv:** Writing – review & editing. **Zhusheng Shi:** Conceptualization, Supervision, Writing – review & editing. **Jianguo Lin:** Conceptualization, Funding acquisition, Writing – review & editing.

Declaration of competing interest

The authors declare that they have no known competing financial interests or personal relationships that could have appeared to influence the work reported in this paper.

Data availability

Data will be made available on request.

Acknowledgements

References

[1] L. Chen, G. Zhao, J. Gong, X. Chen, M. Chen, Hot deformation behaviors and processing maps of 2024 aluminum alloy in as-cast and homogenized states, J. Mater. Eng. Perform. 24 (12) (2015) 5002–5012.

[2] Z. Zhang, W. Zhou, Z. Shi, J. Lin, Advances on manufacture methods for wide lightweight aluminium stiffened panels, in: IOP Conference Series: Materials Science and Engineering, IOP Publishing, 2022, 012122.

[3] H.R. Ashtiani, M. Parsa, H. Bisadi, Constitutive equations for elevated temperature flow behavior of commercial purity aluminum, Mater. Sci. Eng., A 545 (2012) 61–67.

[4] P. Changizian, A. Zarei-Hanzaki, A.A. Roostaei, The high temperature flow behavior modeling of AZ81 magnesium alloy considering strain effects, Mater. Des. 39 (2012) 384–389.

[5] W. Zhou, J. Yu, X. Lu, J. Lin, T.A. Dean, A comparative study on deformation mechanisms, microstructures and mechanical properties of wide thin-ribbed sections formed by sideways and forward extrusion, Int. J. Mach. Tool Manufact. 168 (2021), 103771.

[6] B. Ke, L. Ye, J. Tang, Y. Zhang, S. Liu, H. Lin, Y. Dong, X. Liu, Hot deformation behavior and 3D processing maps of AA7020 aluminum alloy, J. Alloys Compd. 845 (2020), 156113.

[7] O. Sabokpa, A. Zarei-Hanzaki, H. Abedi, N. Haghdadi, Artificial neural network modeling to predict the high temperature flow behavior of an AZ81 magnesium alloy, Mater. Des. 39 (2012) 390–396.

[8] N. Jin, H. Zhang, Y. Han, W. Wu, J. Chen, Hot deformation behavior of 7150 aluminum alloy during compression at elevated temperature, Mater. Char. 60 (6) (2009) 530–536.

[9] W. Li, Y. Liu, S. Jiang, Q. Luan, Y. Li, B. Gu, Z. Shi, A study of thermomechanical behaviour and grain size evolution of AA7050 under hot forging conditions, Int. J. Lightweight Mater. Manuf. 2 (1) (2019) 31–39.

[10] G. Ebrahimi, A. Zarei-Hanzaki, M. Haghshenas, H. Arabshahi, The effect of heat treatment on hot deformation behaviour of Al 2024, J. Mater. Process. Technol. 206 (1–3) (2008) 25–29.

[11] X.H. Fan, M. Li, D.Y. Li, Y.C. Shao, S.R. Zhang, Y.H. Peng, Dynamic recrystallisation and dynamic precipitation in AA6061 aluminium alloy during hot deformation, Mater. Sci. Technol. 30 (11) (2014) 1263–1272.

[12] D. Raabe, M. Sachtleber, H. Weiland, G. Scheele, Z. Zhao, Grain-scale micromechanics of polycrystal surfaces during plastic straining, Acta Mater. 51 (6) (2003) 1539–1560.

[13] C. Yang, X. Wang, S. Yuan, Quantitative analysis of orange peel during tension of 6063 alloy spun tubes, T Nonferr. Metal. Soc. 28 (5) (2018) 858–865.

[14] S.W. Lo, T.C. Horng, Surface roughening and contact behavior in forming of aluminum sheet, J. Tribol. 121 (2) (1999) 224–233.

[15] L. Yang, L. Zhan, W. Wu, Analysis method for orange peel structure on aluminium–lithium alloy surface during stretch forming process, Mater. Res. Innovat. 18 (sup2) (2014). S2-5-S2-11.

[16] V. Romanova, R. Balokhonov, O. Zinovieva, V. Shakhidzhanov, E. Dymnich, O. Nekhorosheva, The relationship between mesoscale deformation-induced surface roughness, in-plane plastic strain and texture sharpness in an aluminum alloy, Eng. Fail. Anal. (2022), 106377.

[17] Z. Feng, H. Li, J. Yang, H. Huang, G. Li, D. Huang, Macro-meso scale modeling and simulation of surface roughening: aluminum alloy tube bending, Int. J. Mech. Sci. 144 (2018) 696–707.

[18] L. Zhang, W. Xu, J. Long, Z. Lei, Surface roughening analysis of cold drawn tube based on macro–micro coupling finite element method, J. Mater. Process. Technol. 224 (2015) 189–199.

[19] D. Rittel, I. Roman, Tensile fracture of coarse-grained cast austenitic manganese steels, Metall. Trans. A 19 A (9) (1988) 2269–2277.

[20] Z. Zhao, R. Radovitzky, A. Cuitino, A study of surface roughening in fcc metals using direct numerical simulation, Acta Mater. 52 (20) (2004) 5791–5804.

[21] O. Wouters, W. Vellinga, R. van Tijum, J.T.M. De Hosson, Effects of crystal structure and grain orientation on the roughness of deformed polycrystalline metals, Acta Mater. 54 (10) (2006) 2813–2821.

[22] E. Emelianova, V. Romanova, O. Zinovieva, R. Balokhonov, The effects of surface-layer grain size and texture on deformation-induced surface roughening in polycrystalline titanium hardened by ultrasonic impact treatment, Mater. Sci. Eng., A 793 (2020), 139896.

[23] J. Zheng, C. Pruncu, K. Zhang, K. Zheng, J. Jiang, Quantifying geometrically necessary dislocation density during hot deformation in AA6082 Al alloy, Mater. Sci. Eng., A 814 (2021), 141158.

[24] T. Yasmeen, S. Rahimi, C. Hopper, C. Zhang, J. Jiang, Unravelling thermal-mechanical effects on microstructure evolution under superplastic forming conditions in a near alpha titanium alloy, J. Mater. Res. Technol. 18 (2022) 4285–4302.

[25] J. Mullin, Crystallization 4, Butterworth-Heinemann, Oxford, 2001.

[26] W. Mao, Recrystallization and grain growth, Handbook of Aluminum 1 (2003) 211–258.

[27] F. Balle, S. Huxhold, S. Emrich, G. Wagner, M. Kopnarski, D. Eifler, Influence of heat treatments on the mechanical properties of ultrasonic welded AA 2024/CF-PA66-Joints, Adv. Eng. Mater. 15 (9) (2013) 837–845.

[28] I. Colour effects, T.P. Woodman, Light scattering in porous anodic aluminium oxide films: I. Colour effects, Thin Solid Films 9 (2) (1972) 195–206.

[29] M.C. Reboul, B. Baroux, Metallurgical aspects of corrosion resistance of aluminium alloys, Mater. Corros. 62 (3) (2011) 215–233.

[30] B.A. Pint, L.R. Walker, I.G. Wright, Factors affecting aluminum depletion during cyclic oxidation of Fe-base alumina-forming alloys, Mater. A. T. High. Temp. 26 (2) (2009) 211–216.

[31] H. Böhni, H. Uhlig, Environmental factors affecting the critical pitting potential of aluminum, J. Electrochem. Soc. 116 (7) (1969) 906.

[32] K. Ralston, N. Birbilis, Effect of grain size on corrosion: a review, Corrosion 66 (7) (2010), 075005-075005-13.

[33] E. Kus, Z. Lee, S. Nutt, F. Mansfeld, A comparison of the corrosion behavior of nanocrystalline and conventional Al 5083 samples, Corrosion 62 (2) (2006) 152–161.

[34] M.K. Chung, Y.S. Choi, J.G. Kim, Y.M. Kim, J.C. Lee, Effect of the number of ECAP pass time on the electrochemical properties of 1050 Al alloys, Mater. Sci. Eng., A 366 (2) (2004) 282–291.

[35] E. Sikora, X. Wei, B. Shaw, Corrosion behavior of nanocrystalline bulk Al-Mg-based alloys, Corrosion 60 (4) (2004).

[36] T. Mahmoud, Effect of friction stir processing on electrical conductivity and corrosion resistance of AA6063-T6 Al alloy, Proc. IME C J. Mech. Eng. Sci. 222 (7) (2008) 1117–1123.

[37] W.R. Osório, C.M. Freire, A. Garcia, The role of macrostructural morphology and grain size on the corrosion resistance of Zn and Al castings, Mater. Sci. Eng., A 402 (1–2) (2005) 22–32.

[38] C. op't Hoog, N. Birbilis, Y. Estrin, Corrosion of pure Mg as a function of grain size and processing route, Adv. Eng. Mater. 10 (6) (2008) 579–582.

[39] H. McQueen, E. Evangelista, N. Jin, M. Kassner, Energy dissipation efficiency in aluminum dependent on monotonic flow curves and dynamic recovery, Metall. Mater. Trans. A 26 (7) (1995) 1757–1766.

[40] H. McQueen, W. Blum, Dynamic recovery: sufficient mechanism in the hot deformation of Al (< 99.99), Mater. Sci. Eng., A 290 (1–2) (2000) 95–107.

[41] H. McQueen, Development of dynamic recrystallization theory, Mater. Sci. Eng., A 387 (2004) 203–208.

[42] H. Yamagata, Dynamic recrystallization of single-crystalline aluminum during compression tests, Scripta Metall. Mater. 27 (6) (1992) 727–732.

[43] J. Lv, J.H. Zheng, V.A. Yardley, Z. Shi, J. Lin, A review of microstructural evolution and modelling of aluminium alloys under hot forming conditions, Metals 10 (11) (2020) 1516.

[44] O. Bembalge, S. Panigrahi, Hot deformation behavior and processing map development of cryorolled AA6063 alloy under compression and tension, Int. J. Mech. Sci. 191 (2021), 106100.

[45] M.R. Stoudt, J.B. Hubbard, S.D. Leigh, On the relationship between deformation-induced surface roughness and plastic strain in aa5052—is it really linear? Metall. Mater. Trans. A 42 (9) (2011) 2668–2679.

[46] N. Wittridge, R. Knutsen, A microtexture based analysis of the surface roughening behaviour of an aluminium alloy during tensile deformation, Mater. Sci. Eng., A 269 (1–2) (1999) 205–216.